Supplementary Information

Deciphering the Molecular Terms of Arp2/3 Allosteric Regulation from All-Atom Simulations and Dynamical Network Theory

Sara Laporte and Alessandra Magistrato*
CNR-IOM at SISSA via Bonomea 265 34136, Trieste, Italy

Correspondence to: alessandra.magistrato@sissa.it

Supplementary Methods

Model Building

The models of Arp2/3 complexes were built on crystal structures deposited in the protein data bank (PDB) (PDBid 3UKR - Arp2/3 bound with CK666, 3ULE - Arp2/3 bound with CK869 and ATP) from *Bovine Thymus*. To dissect the molecular basis of Arp2/3 inhibition by small molecules we considered four models: Arp2/3 in the apo form; Arp2/3 in complex with two ATP molecules; Arp2/3 bound with two ATP molecules and the CK666 inhibitor; and Arp2/3 in complex with two ATP molecules and the CK869 inhibitor. The missing parts of the protein chains were reconstructed by using homology modelling tool of SWISS-MODEL server.[1] The protein structures were assigning the protonation state of the ionizable residues was assessed by using the MAESTRO Schrödinger software suite.[2]

Computational Details

The topology of the system was built with the Amber2018 tool tleap using the AMBER-ff14SB force field (FF).[3] The inhibitors CK666 and CK869 were minimised using Density Functional Theory at the B3LYP level and the 6-31G* basis set. Electrostatic potential (ESP) derived charges were computed according to the Merz-Kolmann partitioning scheme with the Gaussian software.[4] These were then converted to RESP charges with the resp module of Ambertools 2018. The General Amber Force Field (GAFF2) was employed to obtain the other FF parameters,[5] while the ATP parameters were obtained from ref. 6.

The systems were solvated by adding a layer of 30 Å of TIP3P water molecules, resulting in cubic boxes with sides of 170 Å, and neutralized with 1-5 Na^+ ions, using the Joung and Cheatman parameters.[7] Ca^{2+} ions present in the ATP binding sites were described with the Åqvist parameters[8]. Overall each solvated system contained over 484000 atoms. The topologies were subsequently converted in a GROMACS[9] format using the software acpype.[10]

A short minimization was run before annealing the system to 300K. For all simulations the pressure was kept to equilibrium value with the Parrinello-Rahman barostat[11] during the production runs, while the temperature was controlled with the stochastic velocity rescaling thermostat.[12] The LINCS algorithm[13] was used to constrain the bonds involving hydrogen atoms and the particle mesh Ewald method[14] to account for long-range electrostatic interactions with a cutoff of 12 Å. We used an integration time step of 2 fs, and each system underwent an MD simulation of 1 μs reaching 4 μs of cumulative MD simulations.

Analysis

Root mean square deviations (RMSD), principal component analysis (PCA)[15,16] and the per residue correlation matrices were obtained using both GROMACS2018 and Amber 18 programs. In particular the GROMACS2018 tools were used to compute the RMSD (gmx rms), while hydrogen (H-)bond, and cluster analysis, were performed with the AMBER2018 tool *cpptraj*.

In order to monitor the global structural changes occurring in Apr2/3 during the MD simulation we introduce the θ angle, which is defined as the angle between the Cα atoms of residues Phe168, Asp143 and His129 belonging to the C terminal helix of ARPC4.

Principal Component Analysis (PCA) was performed using the *cpptraj* module of Ambertools 18 to extract the essential dynamics of the Arp2/3 models investigated in this study. PCA can capture the large-scale collective motions occurring in biological molecules undergoing MD simulations,[15,16] which allows us to gather information on the major conformational changes occurring along MD trajectories. Mass-weighted covariance matrices were built from the position vectors of the Cα atoms, after an RMS-fit to the starting configuration of the MD production phase, in order to remove the rotational and translational degrees of freedom.[17,18]
In this case the alignment was done on ARPC2 and ARPC4 of the Arp2/3 complex, known to be anchored at the mother actin filament. The eigenvectors characterized by the largest eigenvalues of the matrix describe the most relevant motions sampled during the MD trajectory, usually referred to as principal components (PCs). By projecting the displacement vectors of each atom along the MD trajectory on the principal eigenvector, it is possible to extract the most relevant motions. The Normal Mode Wizard plugin[19] of the Visual Molecular Dynamics (VMD) program has been used for the visualization and analysis of essential dynamics along the principal eigenvectors, and to generate the corresponding images.

The cross-correlation matrices (or normalized covariance matrices) based on the Pearson's correlation coefficients (CCij) were calculated with the *cpptraj* module of Ambertools 18 from the covariance matrices. The matrices have been manipulated by accumulating the correlation for each protein component, by means of correlation scores (CSs) between each protein component and all the others in order to make the matrices clear at first glance. This approach, already introduced to decrypt the correlation pattern of complex biomolecules results in a simplified CCij matrix.[20] To better dissect their role of each a simplified version of the cross-correlation matrix, we considered each protein separately, except Arp2 and Arp3, which were split in two domains. Next, each sum of CSs of pair proteins/domains was divided by the product of the number of residues belonging to this pair of proteins/domains, obtaining as a result a correlation density or each couple of proteins(domains).[21,22] The resulting scores are plotted as matrices showing in a simplified manner the type of correlated motions between each pair of components.

Allosteric paths were investigated using the Weighted Implementation of Suboptimal Paths (WISP) method, which uses dynamical NetWork Analysis (NWA) to find cooperation between protein residues. NWA is done by computing cross-correlations between residues along an MD trajectory enables finding the optimal (most direct path through most correlated residues), and suboptimal communications paths, which also greatly contribute to allosteric communications and provides information about the quality and robustness of the signalling route. The theory and implementation of WISP is detailed in ref. 23.

In the search for paths and for each trajectory, 14000 frames were taken 21 ps apart on the equilibrated part of the trajectory. These frames are then used by the WISP algorithm[23] to construct the optimal path of correlated motions, as well as suboptimal paths, which also contribute to allosteric signalling across the Arp2/3 machinery.

In order to find the path a source and a sink residue defining the beginning and the end of the path need to be defined. The following source and sink residues were chosen to investigate the paths as detailed in the main text:

- source: residue Arg357 on the bumper-helix of Arp3; sink: ATP molecule bound to Arp3.
- source: ATP@Arp3; sink: Arg409 on the C-terminal of Arp3.
- source: Arg409@Arp3; sink: Glu145 at the bend of the long-helix of ARPC4.
- source: residue Arg357@Arp3; sink: residue Arg74 of ARPC1.

Finally, the AllositePro web server[24] was used to identify the presence of druggable pockets across the Arp2/3 structure using a representative structure obtained from cluster analysis of the apo Arp2/3 MD trajectory. The cluster was found to represent 90% of the trajectory. To check for consensus, the same search of allosteric sites was performed on structures obtained from the first half and second half of the same trajectory. Pockets identified were similar in each case. The experimental structures with PDB codes 3UKR and 3ULE were also used to search for allosteric sites, obtaining similar results except for the parts of the protein which are missing, including a part of Arp2, reconstructed for our simulations using homology modelling as stated above.

Supplementary Figures

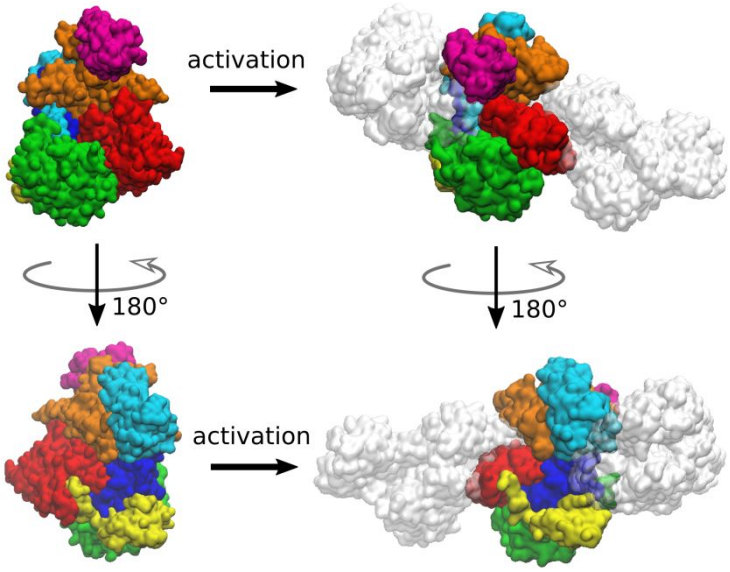

Figure S1: Activating conformational changes of Arp2/3. Arp2/3 is shown in its inactive form (left) and in the active form within a branched actin filament (right). Front and side views are shown (top and bottom). The actin units are shown as transparent white surfaces. Proteins are shown as new cartoons and coloured in green, light-blue, magenta, blue, yellow, red and orange for APRC1, ARPC2, ARPC3, ARPC4, ARPC5, Arp2 and Arp3, respectively. Nucleation of the actin daughter filament occurs at the interface between Arp2 and Arp3, buried in the inactive form and exposed in the active one. Data for the right panel from ref. 25.

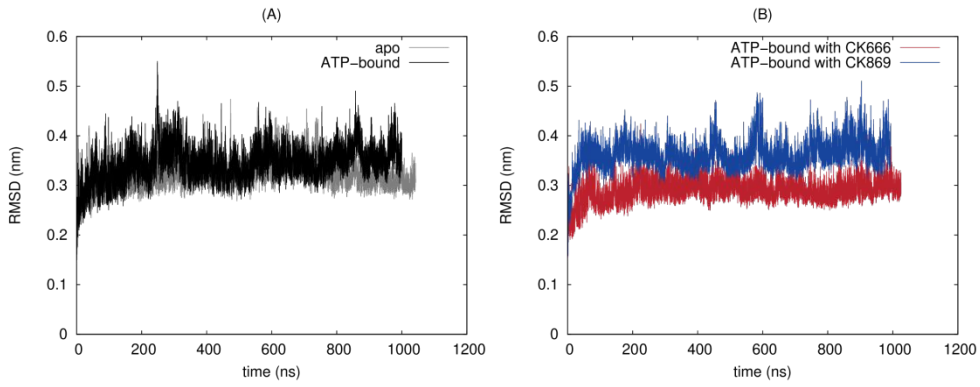

Figure S2. Root mean square displacement (RMSD, nm) calculated on all atoms vs simulations time (ns) for (A) the Arp2/3 in apo and ATP-bound forms, and (B) ATP-bound Arp2/3 in complex with the CK666 and CK869 inhibitors. The large RMSD value is due to the high mobility of the machinery. The least mobile parts of Arp2/3 were found to be ARPC2 and ARPC4, whose RMSD when computed alone stabilises at around 17 Å.

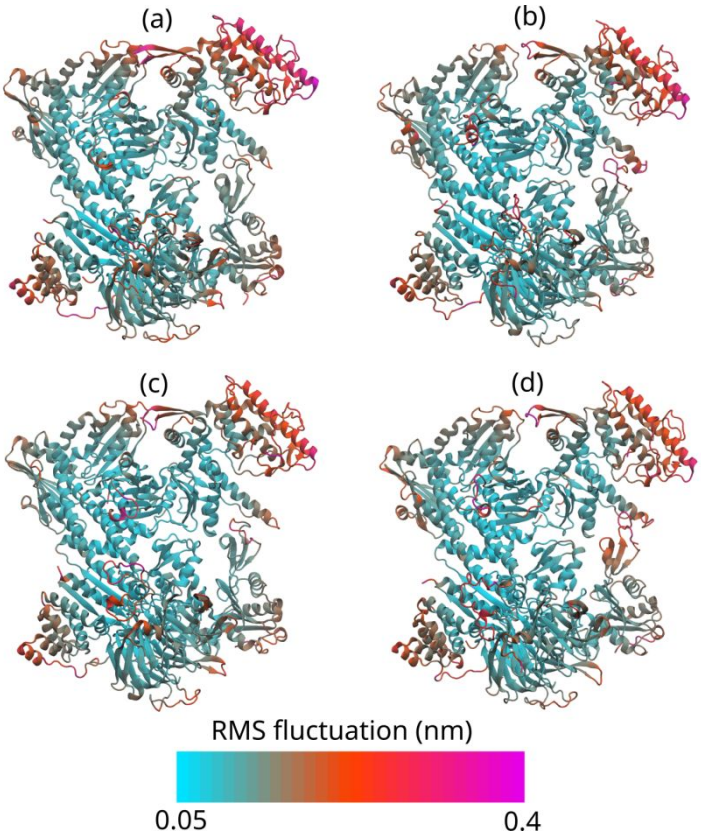

Figure S3. Root mean square fluctuations (nm) for the Arp2/3 apo (a), Arp2/3 in complex with two ATP molecules (b), Arp2/3 in complex with two ATP molecules and CK666 (c), Arp2/3 bound to two ATP molecules and CK666 (d), and Arp2/3 bound to two ATP molecules and CK869 (e).

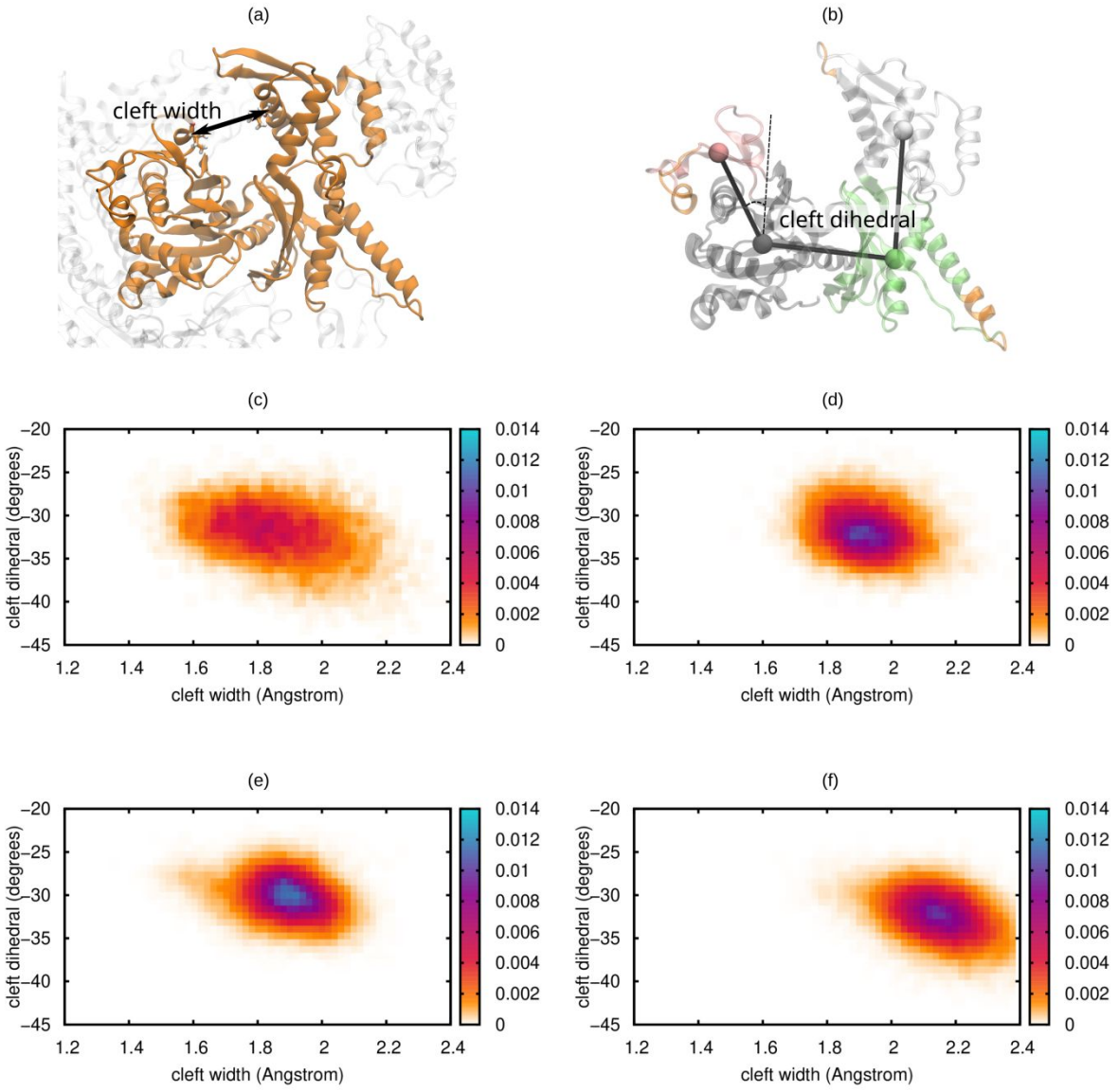

Figure S4: (a) Definition of the ATP binding cleft width, between the Cα atoms of Lys69 and Ala224 residues, and (b) of the binding-cleft twist. The twist angle of the binding-cleft is defined by the center of masses Arp3's domains: domain 2 (pink) residues 32-37 and 50-75, domain 1 (black) residues 1-31, 76-152, and 369-414, domain 3 (lime) residues 153-195, 290-345, and 356-368, domain 4 (white) residues 196-290. Domains are defined with respect to those in present in actin monomers,[26] and inserts that are specific to Arp3 have been left out due to their high flexibility (shown as orange on the figure). 2D distributions of the nucleotide binding cleft width and dihedral (c) apo, (d) ATP-bound, (e) ATP and CK666-bound, (f) ATP and CK869 bound-Arp2/3.

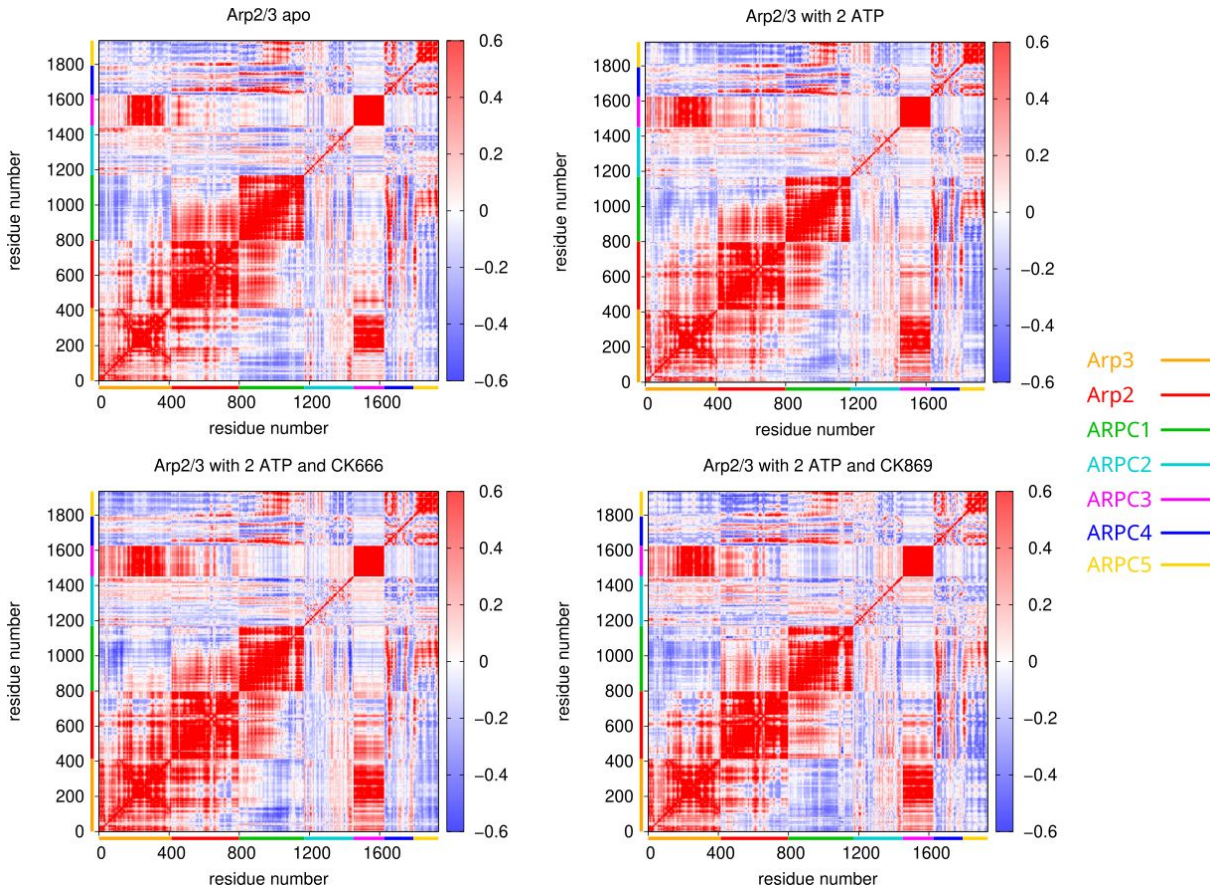

Figure S5. Cooperative motion underlying the functional dynamics of the distinct Arp2/3 models. The per-residue Pearson's coefficient (CCs) cross-correlation matrix is derived from the mass-weighted covariance matrix calculated over the last 900 ns of classical molecular dynamics trajectories. CCs values range from −0.6 (blue, anti-correlated motions) to +0.6 (red, correlated motions). Protein names are labelled on the bottom and left of the matrix and reported in the same colour code of Figure 1. Residues are numbers as if a single chain.

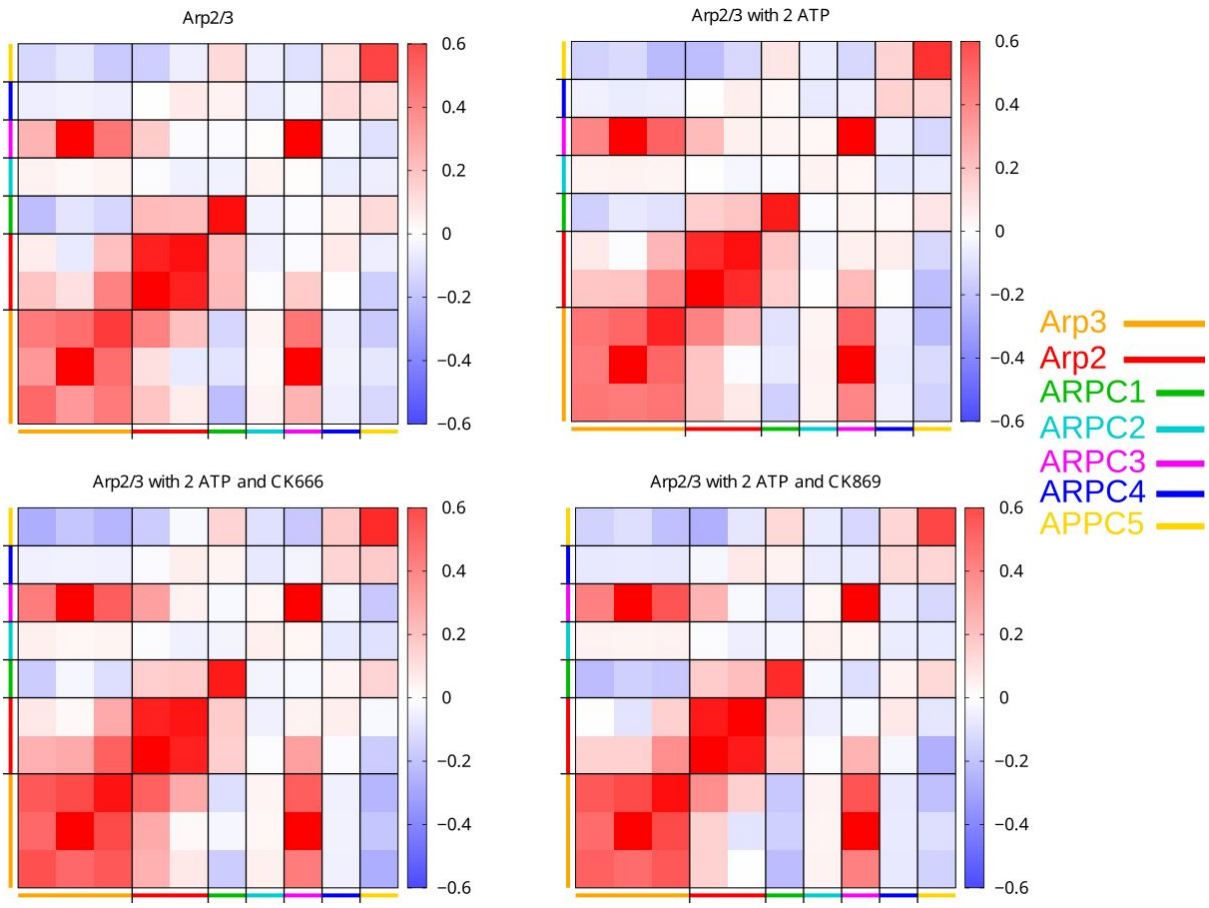

Figure S6. Cross-correlation matrix averages over protein domains (2 domains for Arp2 and Arp3, and one domain per protein for ARPC1-5). Values range from -0.6 (blue, anti-correlated motion) to +0.6 (red, correlated motion). Protein names are labelled on the bottom left using the same colour-code as in previous figures. The splitting of Arp2 and Arp3 corresponds to the "large" and "small" domains of actin-like proteins,[26] as shown in Figure S4 (lime and white residues 1-195, pink and black residues 196-414). In the apo form, while Arp3 moves lockstep with ARPC2 and ARPC3, and Arp2 weakly positively correlates with ARPC2, and negatively correlates with ARPC1. Arp2 is divided in two dynamical domains around residue Gly201 which corresponds to the pivot between Arp2 and Arp3 motion. The relevance of this residue is remarked by the fact that in all cases studied Gly201@Arp2 establishes an H-bond with Arg123@Arp3 (Table S2), and both inhibitors interact with this zone (CK666 with Asp209@Arp2, and CK869 with Asn122@Arp3, Table S1).

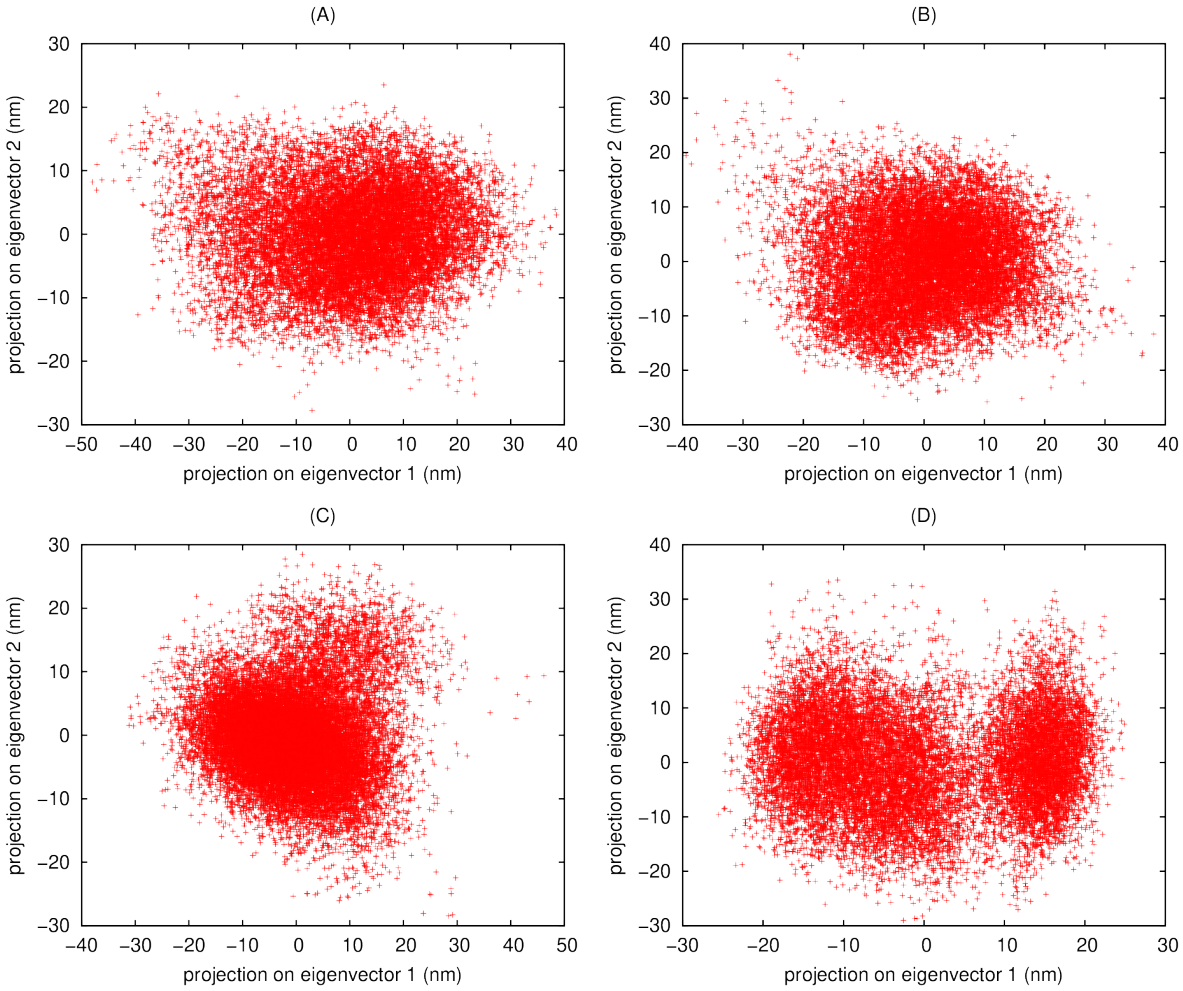

Figure S7. Scatter plot reporting principal component 1 (PC1) vs PC2 for the Arp2/3 apo (A), Arp2/3 in complex with two ATP molecules (B), Arp2/3 in complex with two ATP molecules and CK666 (C) and Arp2/3 bound to two ATP molecules and CK869 (D).

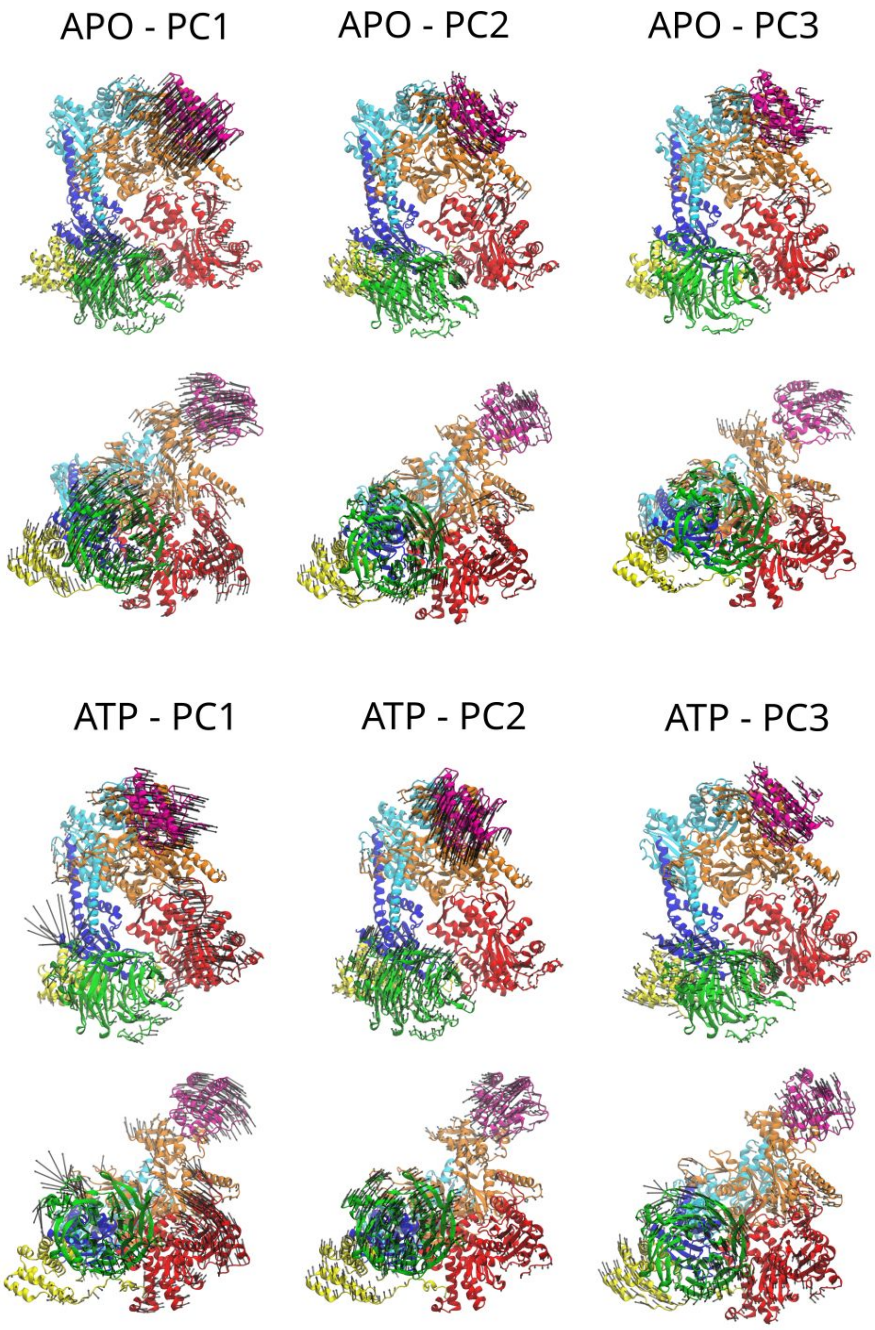

Figure S8. Principal Component (PC) 1, 2 and 3 of the apo and ATP-bound complex, with the motion represented by arrows on Cα carbons of Arp2/3. Proteins are shown as new cartoons and coloured in green, light blue, magenta, blue, yellow, red and orange for APRC1, ARPC2, ARPC3, ARPC4, ARPC5, Arp2 and Arp3, respectively.

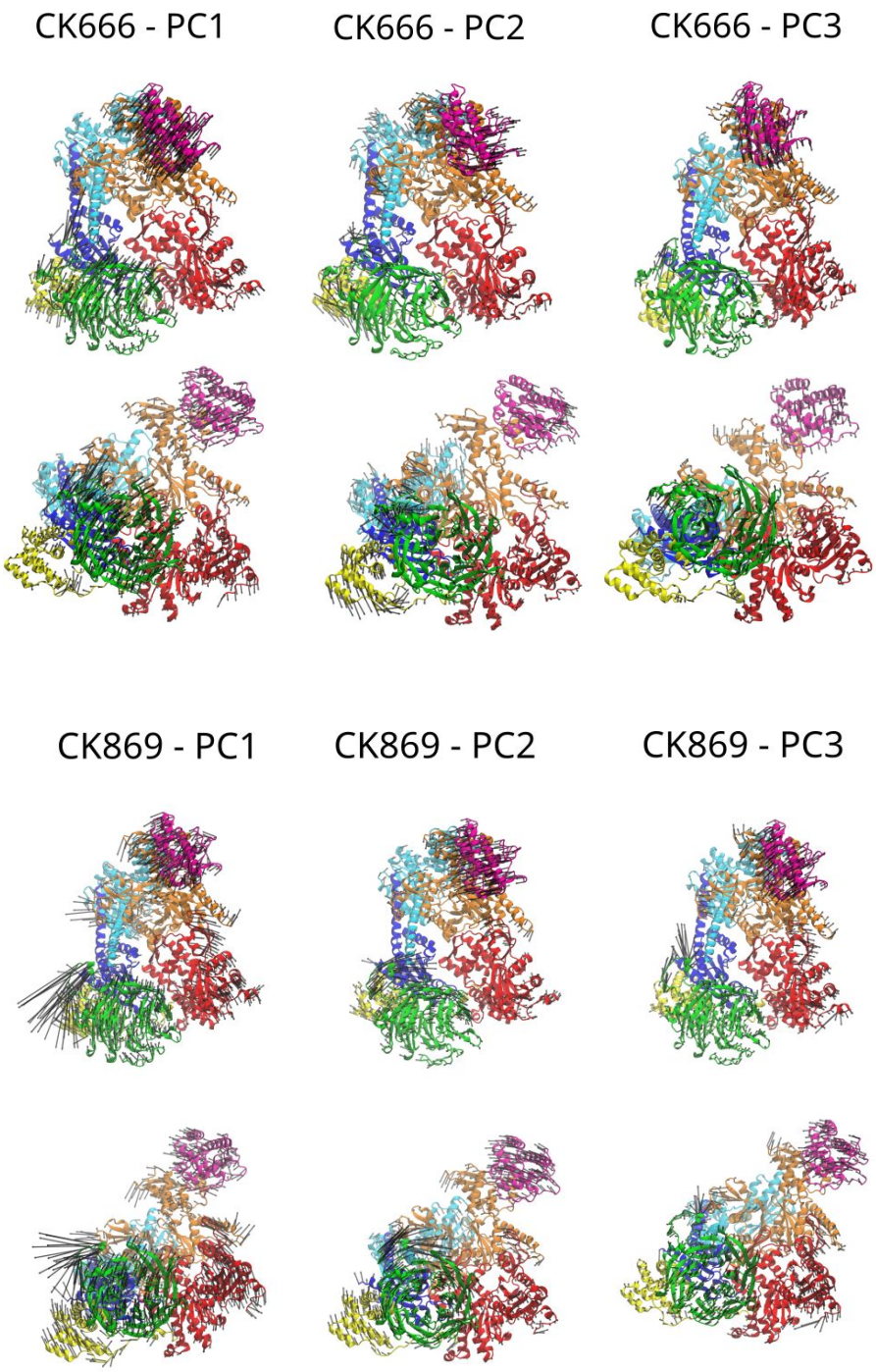

Figure S9. Principal Component (PC) 1, 2 and 3 of the CK666- and CK869-bound complex, with the motion represented by arrows on Cα carbons of Arp2/3. Proteins are shown as new cartoons and coloured in green, light blue, magenta, blue, yellow, red and orange for APRC1, ARPC2, ARPC3, ARPC4, ARPC5, Arp2 and Arp3, respectively.

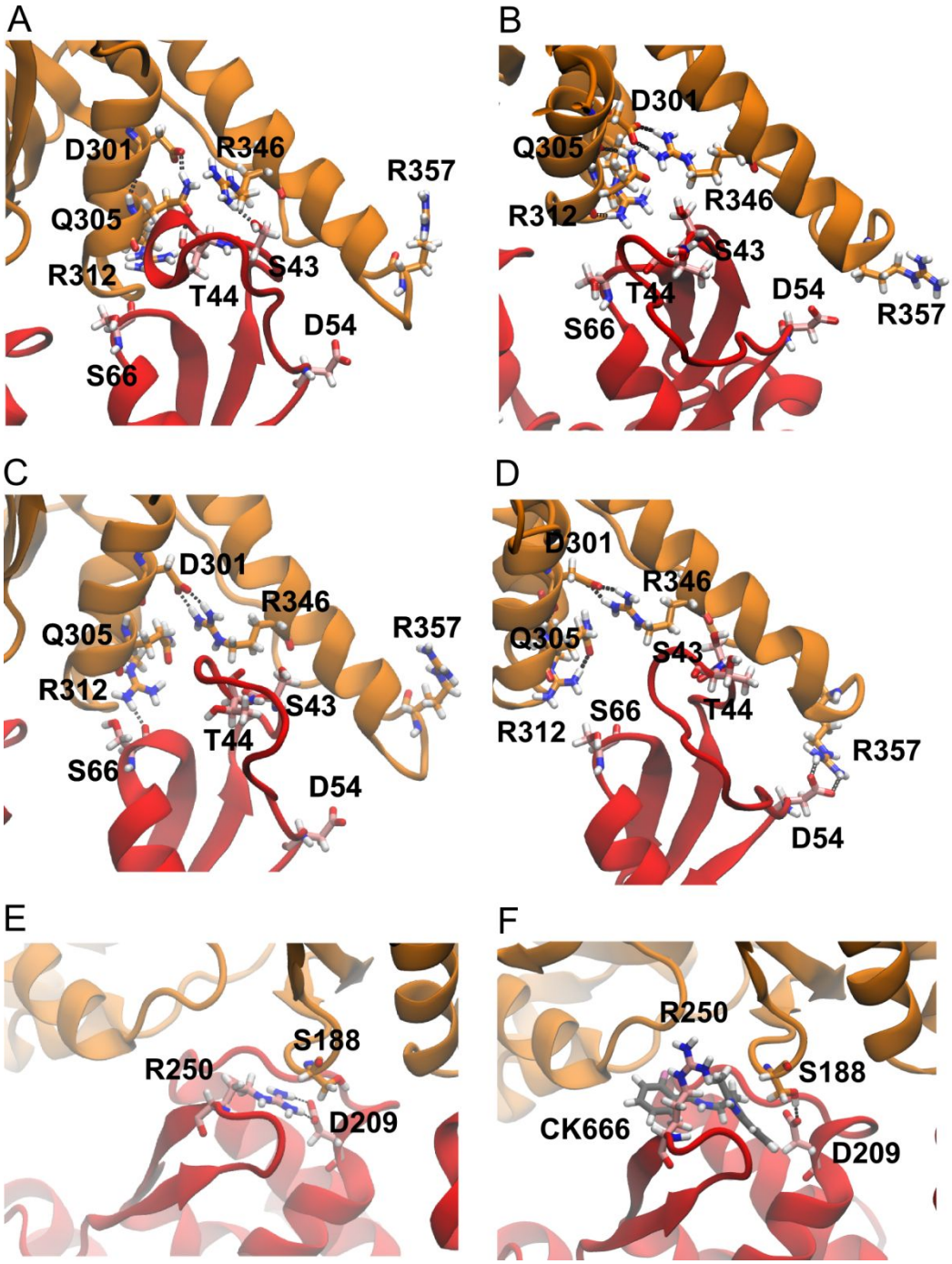

Figure S10. Representative frames from the classical MD trajectory of the Arp2/Arp3 interface at the bumper-helix for A) apo, B) ATP-bound, C) ATP and CK666-bound and D) ATP and CK869-bound complex. Key residues are represented as labelled. Persistent hydrogen bond network is shown as black dashed lines (F).

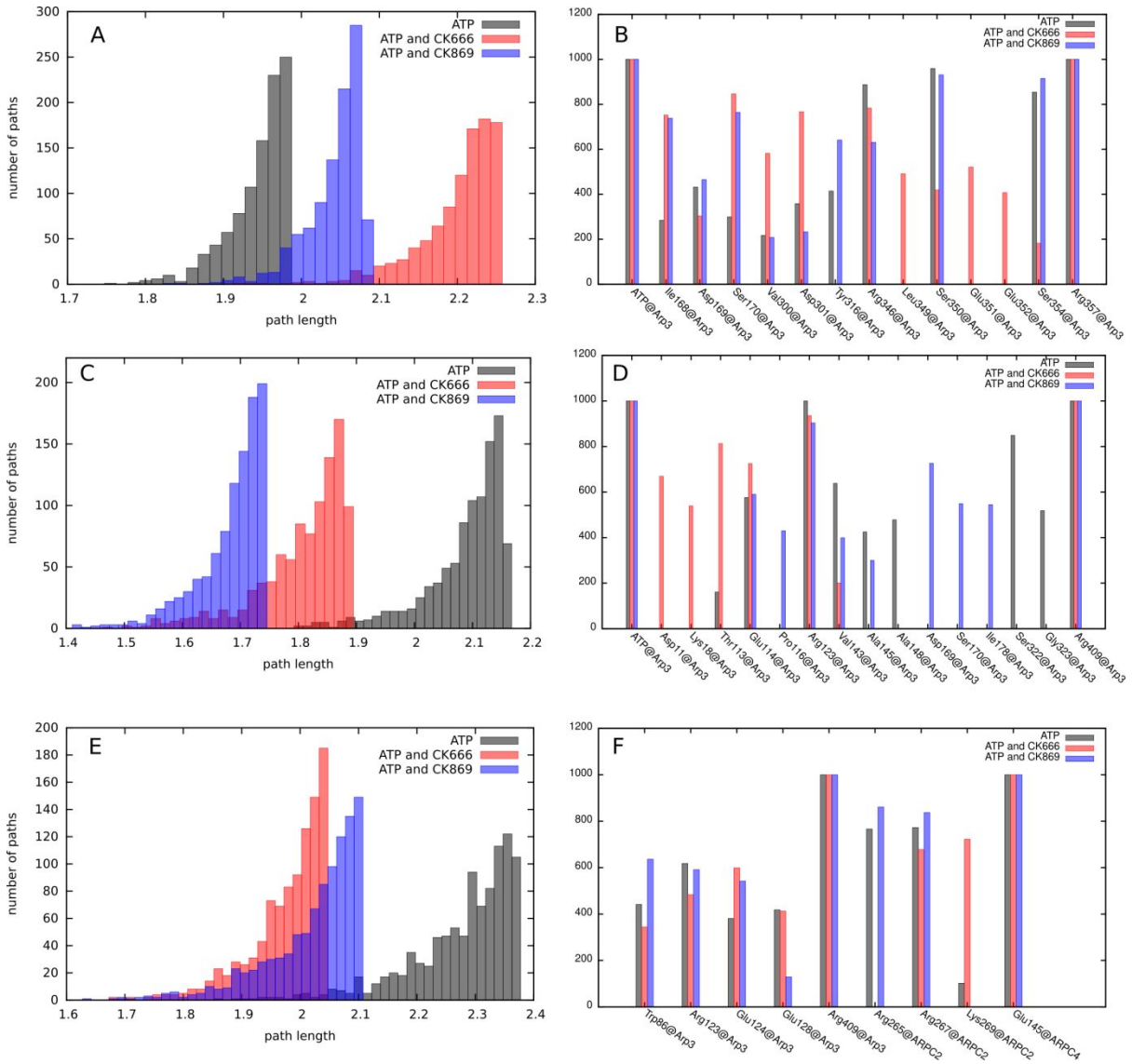

Figure S11. Histograms of path lengths (A, C, E) of the 1000 shortest paths reported in Figure 4 of the main text. Degeneracy of the residues present in the given path (B, D, and F). Only residues present in at least 400 paths are shown.

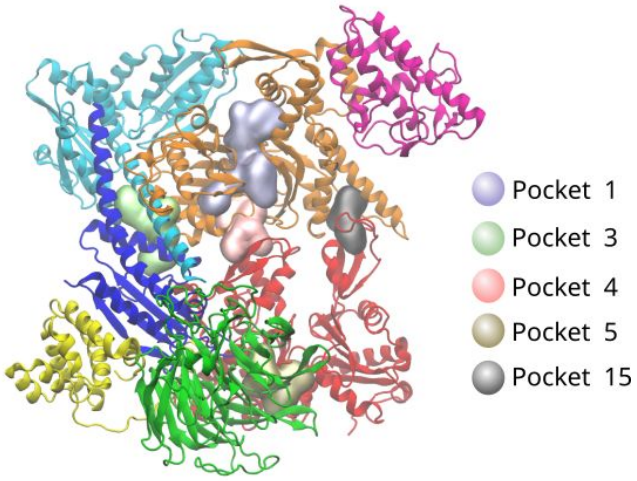

Figure S12. Druggable allosteric sites: pockets are depicted as translucent surfaces. Pockets 1, 3, 4, 5 and 15 are shown as purple, lime, pink, gold and black surface, respectively. Pocket 1 coincides with the Arp3's ATP binding cleft. Proteins are shown as new cartoons and coloured in green, light blue, magenta, blue, yellow, orange and red for APRC1, ARPC2, ARPC3, ARPC4, ARPC5, ARP2, ARP3, respectively. As stated in the methods section, other representative structures were submitted to the allosteric pocket search, yielding only small variations in pockets found. In some cases, the ATP@Arp3 and CK869 sites are found separately, making the site with the highest volume the ATP@Arp2 site (not shown).

Supplementary Tables

Table S1. Persistence of selected hydrogen bonds calculated as the number of frames the hydrogen bond is present with respect to the total simulation time

Donor residue	Acceptor residue	apo	ATP	CK666	CK869
CK666	Arp2 ASP 248	N/A	N/A	0.9	N/A
Arp3 ARG 346	Arp3 ASP 301	-	0.95	0.97	0.93
Arp3 ARG 357	Arp2 ASP 54	-	0.18	-	0.8
Arp3 ARG 312	Arp2 SER 66	0.1	0.2	1.0	0.3
Arp2 ARG 250	Arp2 ASP 209	0.6	0.6	-	0.55
Arp3 SER 188	Arp2 ASP 209	-	0.38	0.87	-
Arp3 ARG 123	Arp2 GLY 201	0.85	0.8	0.75	0.66
ARPC2 ARG 265	ARPC4 GLU 145	0.01	0.9	0.14	0.9
ARPC1 ARG 74	Arp2 ASP 346	0.9	0.9	0.9	0.7
ARPC1 ARG 74	ARPC4 GLU 31	0.7	0.87	0.83	0.3

Table S2. Total the binding free energy and per-residue contribution to the binding free energy (kcal/mol) of CK666 (a) and CK869 (b) as obtained from Molecular Mechanics Generalized Born Surface Area calculations (MM-GBSA).[27] The electrostatic and van der Waals contributions to the total binding free energy are also listed.

(a)

Residue	*van der Waals*	*Electrostatic*	***TOTAL***
Arp3 LEU 117	-2.0±0.5	-0.5±0.2	**-2.2±0.5**
Arp3 GLY 187	-0.9±0.3	-0.6±0.2	**-1.3±0.4**
Arp3 SER 188	-1.6±0.7	-0.8±0.3	**-2.5±0.9**
Arp2 ASP 209	-1.2±0.2	1.6±0.6	**2.3±1.1**
Arp2 LEU 246	-2.2±0.3	-0.4±0.2	**-2.6±0.4**
Arp2 ASP 248	-0.6±0.6	-8.0±0.9	**-6.0±0.6**
Arp2 ARG 250	-2.0±0.3	3.6±0.5	**0.9±0.5**
Arp 2 ILE 252	-0.9±0.2	-0.2±0.1	**-1.0±0.2**
TOTAL	-43.9±0.3	-5.2±0.1	**-21.7±0.3**

(b)

Residue	*van der Waals*	*Electrostatic*	***TOTAL***
Arp3 ASP 11	-0.1±0.0	-1.5±0.2	**-1.3±0.3**
Arp3 CYS 12	-0.9±0.0	-0.5±0.2	**-1.0±0.3**
Arp3 LYS 18	0.0±0.0	1.2±0.2	**0.9±0.2**
Arp3 TRP 86	-1.2±0.2	-0.2±0.2	**-1.4±0.3**
Arp3 MET 89	-2.5±0.4	-0.5±0.3	**-2.9±0.5**
Arp3 MET 93	-0.8±0.2	-0.3±0.2	**-1.1±0.3**
Arp3 LEU 112	-1.9±0.4	0.0±0.2	**-1.9±0.3**
Arp3 THR 113	-1.1±0.2	-1.1±0.4	**-1.4±0.4**
Arp3 GLU 114	-1.7±0.2	-0.4±0.9	**-1.9±0.9**
Arp3 ASN 118	-0.3±0.4	-2.0±0.7	**-2.2±0.5**
Arp3 ASN 122	-1.1±0.2	-2.1±0.5	**-2.8±0.6**
Arp3 ARG 123	-0.9±0.2	-0.5±0.5	**-1.2±0.4**
Arp3 GLU 124	-0.1±0.0	0.7±0.2	**0.5±0.2**
Arp3 THR 126	-1.8±0.4	-1.1±0.3	**-2.5±0.6**
Arp3 ILE 141	-1.0±0.2	0.0±0.1	**-1.0±0.2**
TOTAL	-45.4±0.2	-3.5±0.1	**-18.3±2.6**

Table S3. Allosteric sites scores, corresponding to the sites depicted in Figure S12 are listed according to volumes detected by the AlloSitePro server.[24] SASA stands for solvent accessible surface area. Among the allosteric sites identified, Pocket 1 has the highest volume and SASA scores and includes the ATP binding pocket and the CK869 binding site, thus coinciding with a critical modulatory region of the machinery, and confirming the quality of the prediction.

Pocket number	Volume	SASA	Drugability Score	Overall score
1 (highest volume)	2347.147	1147.971	0.068	0.774
3 (high overall score)	1021.135	537.287	0.112	0.869
4 (highest overall score)	980.303	539.593	0.213	0.885
5 (high drugability)	921.904	512.335	0.257	0.817
15 (highest drugability)	491.87	212.697	0.272	0.783

Supplementary Movies

Movies can be found at:
https://drive.google.com/drive/folders/1k9ymCYZJtqMdYYYl5_p2eS8mJ6Y-b-qH?usp=sharing.
Proteins are shown as new cartoons and coloured in green, light blue, magenta, blue, yellow, orange and red for APRC1, ARPC2, ARPC3, ARPC4, ARPC5, ARP2, ARP3, respectively. For each PC, the side or bottom view has been selected to show the most obvious amplitude of movement.

- S1.mp4: PC1 of apo Arp2/3
- S2.mp4: PC2 of apo Arp2/3
- S3.mp4: PC1 of ATP-bound Arp2/3
- S4.mp4: PC2 of ATP-bound Arp2/3
- S5.mp4: PC3 of ATP-bound Arp2/3
- S6.mp4: PC1 of CK666-inhibited Arp2/3 form
- S7.mp4: PC2 of CK666-inhibited Arp2/3 form
- S8.mp4: PC1 of CK869-inhibited Arp2/3 form
- S9.mp4: PC2 of CK869-inhibited Arp2/3 form

References

(1) Waterhouse, A.; Bertoni, M.; Bienert, S.; Studer, G.; Tauriello, G.; Gumienny, R.; Heer, F. T.; de Beer, T. A. P.; Rempfer, C.; Bordoli, L.; Lepore, R.; Schwede, T. SWISS-MODEL: Homology Modelling of Protein Structures and Complexes. *Nucleic Acids Res.* **2018**, *46* (W1), W296–W303.

(2) *Maestro*; Schrödinger LLC: New York, NY, 2020.

(3) Maier, J. A.; Martinez, C.; Kasavajhala, K.; Wickstrom, L.; Hauser, K. E.; Simmerling, C. Ff14SB: Improving the Accuracy of Protein Side Chain and Backbone Parameters from Ff99SB. *J. Chem. Theory Comput.* **2015**, *11* (8), 3696–3713.

(4) Frisch, M. J.; Trucks, G. W.; Schlegel, H. B.; Scuseria, G. E.; Robb, M. A.; Cheeseman, J. R.; Scalmani, G.; Barone, V.; Petersson, G. A.; Nakatsuji, H.; Li, X.; Caricato, M.; Marenich, A. V.; Bloino, J.; Janesko, B. G.; Gomperts, R.; Mennucci, B.; Hratchian, H. P.; Ortiz, J. V.; Izmaylov, A. F.; Sonnenberg, J. L.; Williams; Ding, F.; Lipparini, F.; Egidi, F.; Goings, J.; Peng, B.; Petrone, A.; Henderson, T.; Ranasinghe, D.; Zakrzewski, V. G.; Gao, J.; Rega, N.; Zheng, G.; Liang, W.; Hada, M.; Ehara, M.; Toyota, K.; Fukuda, R.; Hasegawa, J.; Ishida, M.; Nakajima, T.; Honda, Y.; Kitao, O.; Nakai, H.; Vreven, T.; Throssell, K.; Montgomery Jr., J. A.; Peralta, J. E.; Ogliaro, F.; Bearpark, M. J.; Heyd, J. J.; Brothers, E. N.; Kudin, K. N.; Staroverov, V. N.; Keith, T. A.; Kobayashi, R.; Normand, J.; Raghavachari, K.; Rendell, A. P.; Burant, J. C.; Iyengar, S. S.; Tomasi, J.; Cossi, M.; Millam, J. M.; Klene, M.; Adamo, C.; Cammi, R.; Ochterski, J. W.; Martin, R. L.; Morokuma, K.; Farkas, O.; Foresman, J. B.; Fox, D. J. *Gaussian 16 Rev. C.01*; Wallingford, CT, 2016.

(5) Wang, J.; Wolf, R. M.; Caldwell, J. W.; Kollman, P. A.; Case, D. A. Development and Testing of a General Amber Force Field. *J. Comput. Chem.* **2004**, *25* (9), 1157–1174.

(6) Meagher, K. L.; Redman, L. T.; Carlson, H. A. Development of Polyphosphate Parameters for Use with the AMBER Force Field. *J. Comput. Chem.* **2003**, *24* (9), 1016–1025.

(7) Joung, I. S.; Cheatham, T. E. Determination of Alkali and Halide Monovalent Ion Parameters for Use in Explicitly Solvated Biomolecular Simulations. *J. Phys. Chem. B* **2008**, *112* (30), 9020–9041.

(8) Åqvist, J. Ion-Water Interaction Potentials Derived from Free Energy Perturbation Simulations. *J. Phys. Chem.* **1990**, *94* (21), 8021–8024.

(9) Van Der Spoel, D.; Lindahl, E.; Hess, B.; Groenhof, G.; Mark, A. E.; Berendsen H. J. C. GROMACS: Fast, Flexible, and Free. *J. Comput. Chem.* **2005**, *26*, 1701-1718.

(10) Sousa da Silva, A. W.; Vranken, W. F. ACPYPE - AnteChamber PYthon Parser InterfacE. *BMC Res. Notes* **2012**, *5* (1), 367.

(11) Parrinello, M.; Rahman, A. Crystal Structure and Pair Potentials: A Molecular-Dynamics Study. *Phys. Rev. Lett.* **1980**, *45* (14), 1196–1199.

(12) Bussi, G.; Donadio, D.; Parrinello, M. Canonical Sampling through Velocity Rescaling. *J. Chem. Phys.* **2007**, *126* (1), 014101.

(13) Hess, B.; Bekker, H.; Berendsen, H. J. C.; Fraaije, J. G. E. M. LINCS: A Linear Constraint Solver for Molecular Simulations. *J. Comput. Chem.* **1997**, *18* (12), 1463–

1472.
(14) Darden, T.; York, D.; Pedersen, L. Particle Mesh Ewald: An N·log(N) Method for Ewald Sums in Large Systems. *J. Chem. Phys.* **1993**, *98* (12), 10089–10092.
(15) David, C. C.; Jacobs, D. J. Principal Component Analysis: A Method for Determining the Essential Dynamics of Proteins. In *Protein Dynamics: Methods and Protocols*; Livesay, D. R., Ed.; Methods in Molecular Biology; Humana Press: Totowa, NJ, 2014; pp 193–226.
(16) Amadei, A.; Linssen, A. B.; Berendsen, H. J. Essential Dynamics of Proteins. *Proteins* **1993**, *17* (4), 412–425.
(17) Casalino, L.; Palermo, G.; Spinello, A.; Rothlisberger, U.; Magistrato, A. All-Atom Simulations Disentangle the Functional Dynamics Underlying Gene Maturation in the Intron Lariat Spliceosome. *Proc. Natl. Acad. Sci.* **2018**, *115* (26), 6584–6589.
(18) Saltalamacchia, A.; Casalino, L.; Borišek, J.; Batista, V. S.; Rivalta, I.; Magistrato, A. Decrypting the Information Exchange Pathways across the Spliceosome Machinery. *J. Am. Chem. Soc.* **2020**, *142* (18), 8403–8411.
(19) Bakan, A.; Meireles, L. M.; Bahar, I. ProDy: Protein Dynamics Inferred from Theory and Experiments. *Bioinformatics* **2011**, *27* (11), 1575–1577.
(20) Pavlin, M.; Spinello, A.; Pennati, M.; Zaffaroni, N.; Gobbi, S.; Bisi, A.; Colombo, G.; Magistrato, A. A Computational Assay of Estrogen Receptor α Antagonists Reveals the Key Common Structural Traits of Drugs Effectively Fighting Refractory Breast Cancers. *Sci. Rep.* **2018**, *8* (1), 649.
(21) Borišek, J.; Saltalamacchia, A.; Gallì, A.; Palermo, G.; Molteni, E.; Malcovati, L.; Magistrato, A. Disclosing the Impact of Carcinogenic SF3b Mutations on Pre-MRNA Recognition Via All-Atom Simulations. *Biomolecules* **2019**, *9* (10), 633.
(22) Borišek, J.; Saltalamacchia, A.; Spinello, A.; Magistrato, A. Exploiting Cryo-EM Structural Information and All-Atom Simulations To Decrypt the Molecular Mechanism of Splicing Modulators. *J. Chem. Inf. Model.* **2020**, *60* (5), 2510–2521.
(23) Van Wart, A. T.; Durrant, J.; Votapka, L.; Amaro, R. E. Weighted Implementation of Suboptimal Paths (WISP): An Optimized Algorithm and Tool for Dynamical Network Analysis. *J. Chem. Theory Comput.* **2014**, *10* (2), 511–517.
(24) Huang, W.; Lu, S.; Huang, Z.; Liu, X.; Mou, L.; Luo, Y.; Zhao, Y.; Liu, Y.; Chen, Z.; Hou, T.; Zhang, J. Allosite: A Method for Predicting Allosteric Sites. *Bioinformatics* **2013**, *29* (18), 2357–2359.
(25) Pfaendtner, J.; Volkmann, N.; Hanein, D.; Dalhaimer, P.; Pollard, T. D.; Voth, G. A. Key Structural Features of the Actin Filament Arp2/3 Complex Branch Junction Revealed by Molecular Simulation. *J. Mol. Biol.* **2012**, *416* (1), 148–161.
(26) Dominguez, R; Holmes, K. C. Actin Structure and Function. *Annu. Rev. Biophys.* **2011**, *40,*169–86.
(27) Massova, I.; Kollman, P. A. Combined Molecular Mechanical and Continuum Solvent Approach (MM-PBSA/GBSA) to Predict Ligand Binding. *Persp. Drug Discov.* **2000**, *18*, 113-135.